Available online at www.sciencedirect.com

ScienceDirect

Geochimica et Cosmochimica Acta 294 (2021) 255–272

Geochimica et Cosmochimica Acta

www.elsevier.com/locate/gca

Scandium immobilization by goethite: Surface adsorption versus structural incorporation

Hai-Bo Qin [a,b,*], Shitong Yang [c], Masato Tanaka [a], Kenzo Sanematsu [d], Carlo Arcilla [e], Yoshio Takahashi [a,*]

[a] Department of Earth and Planetary Science, Graduate School of Science, The University of Tokyo, Hongo 7-3-1, Bunkyo-ku, Tokyo 113-0033, Japan

[b] State Key Laboratory of Environmental Geochemistry, Institute of Geochemistry, Chinese Academy of Sciences, Guiyang 550081, China

[c] School of Human Settlements and Civil Engineering, Xi'an Jiaotong University, Xi'an 710049, PR China

[d] Institute for Geo-Resources and Environment, National Institute of Advanced Industrial Science and Technology, Central 7, 1-1-1 Higashi, Tsukuba, Ibaraki 305-8567, Japan

[e] Department of Science and Technology, Philippine Nuclear Research Institute, Central Avenue, Quezon City 1101, Philippines

Received 24 June 2020; accepted in revised form 21 November 2020; available online 27 November 2020

Abstract

Several recent studies have reported a strong association between Sc and goethite (α-FeOOH) in synthetic analogs and natural samples. However, the mechanism of Sc immobilization by goethite and controlling factors remain unclear. This study investigated the adsorption behavior and molecular-scale immobilization mechanisms of Sc at water/goethite interfaces through a combination of batch adsorption and desorption experiments, X-ray absorption fine structure (XAFS) analyses, and density functional theory (DFT) calculations. Results indicate that Sc is preferentially adsorbed on goethite with the formation of bidentate-binuclear inner-sphere complexes at the corner-sharing sites. Bulk Sc K-edge XAFS analyses suggest that Sc is incorporated into the goethite structure by substituting for Fe(III) within the crystal in synthetic Sc-substituted goethite, which is further confirmed in natural goethite particles in the laterite by using micro-focused XAFS (μ-XAFS). Furthermore, we demonstrate that the adsorbed Sc on the goethite surface can be structurally incorporated into the goethite lattice in the presence of aqueous Fe(II) possibly through goethite recrystallization induced by aqueous Fe(II). This process may affect the (re)partitioning of Sc between the goethite surface and the mineral bulk, which could be used to rationally explain disparate Sc speciation in laterites from different regions. Our study elucidates the molecular-scale mechanisms underlying Sc adsorption on and structural incorporation into goethite, providing critical insights into the understanding of geochemical behavior and environmental fates of Sc.

Keywords: Scandium (Sc); Goethite (α-FeOOH); Substitution; Adsorption; Molecular mechanism; X-ray absorption fine structure (XAFS)

1. INTRODUCTION

Scandium (Sc) is a critical metal with wide industrial applications, such as in Al-Sc alloys for the aerospace and automotive industries, in solid oxide fuel cells (SOFC), and in the electronic industry (US Geological Survey, 2020). The growing demands have recently attracted an increasing interest with respect to Sc resources. In

* Corresponding authors at: State Key Laboratory of Environmental Geochemistry, Institute of Geochemistry, Chinese Academy of Sciences, Guiyang 550081, China (H.-B. Qin).

E-mail addresses: qinhaibo@vip.gyig.ac.cn (H.-B. Qin), ytakaha@eps.s.u-tokyo.ac.jp (Y. Takahashi).

https://doi.org/10.1016/j.gca.2020.11.020

particular, the laterite shows a great potential as a new (by-product) resource of Sc (e.g., Wang et al., 2011; Chassé et al., 2017; Williams-Jones and Vasyukova, 2018; Orberger and van der Ent, 2019; Ulrich et al., 2019). Nonetheless, little is known about the geochemical behavior and environmental fates of Sc because of its scarce accumulation in nature. The identification of Sc speciation in complex natural systems remains challenging due to the scarcity of direct Sc structural data and the poor understanding of Sc K-edge X-ray absorption near-edge structure (XANES) reference spectra (Chassé et al., 2018).

Iron (oxyhydr)oxides, such as goethite (α-FeOOH), hematite, and ferrihydrite, are ubiquitous in soils, ore deposits (e.g., laterites), and continental and marine sediments (e.g., ferromanganese nodules). The uptake of trace elements (e.g., Ni, Cd, Se, Te, As, and Sb) by these Fe (III) (oxyhydr)oxide minerals plays an important role in the control of geochemical behavior and environmental fates of the metal(loid)s (Takahashi et al., 2007, 2015; Harada and Takahashi, 2008; Brown and Calas, 2013; Qin et al., 2017a, 2019). In the case of Sc, a strong association with goethite has been recently demonstrated in synthetic analogs and natural samples (e.g., Chassé et al., 2017, 2019; Vind et al., 2018; Ulrich et al., 2019). Nevertheless, the interaction between Sc and goethite is still poorly understood and remains debated. By using XANES analysis, the pioneering study by Chassé et al. (2017) showed that Sc speciation in the lateritic duricrusts in eastern Australia is dominated by species adsorbed on goethite along with a small amount of substituted species in the hematite structure. By contrast, several studies have demonstrated that the structural incorporation of Sc into goethite could be the critical Sc species in laterites (Muñoz et al., 2017; Ulrich et al., 2019; Qin et al., 2020). Indeed, a continuous $Fe_xSc_{(1-x)}OOH$ solid solution has been synthesized in the laboratory (Levard et al., 2018). Thus, the adsorption and incorporation processes of Sc by goethite could play critical roles in the control of speciation and distribution of Sc in the environment. However, the mechanisms of Sc immobilization by goethite and controlling factors remain unclear.

Goethite recrystallization has been proposed as a fundamental geochemical process affecting the cycling of various trace elements (e.g., Catalano et al., 2011; Frierdich et al., 2011, 2019a; Hinkle and Catalano; 2015; Burton et al., 2020), although this process occurs slowly under oxidizing conditions where the solubility of goethite is low. Nonetheless, aqueous Fe(II) can catalyze goethite recrystallization rapidly via Fe atom exchange under reducing conditions, as clearly demonstrated by an Fe isotope tracer and 3D atom probe tomography (APT) approach (Handler et al., 2009, 2014; Frierdich et al., 2014, 2019b; Taylor et al, 2019). During aqueous Fe(II)-activated recrystallization, some trace elements (e.g., Ni and Sb) adsorbed on the goethite surface can be progressively incorporated into the crystal structure (e.g., Frierdich et al., 2011; Burton et al., 2020). Previous studies on Fe geochemical cycles in laterites indicated that Fe is mobile in the forms of Fe (II)-rich groundwater and soil water during lateritization, although aqueous Fe(II) can be oxidized to Fe(III)-(oxyhydr)oxides (e.g., goethite) by molecular oxygen during dry seasons (Beukes et al., 2002; Yamaguchi et al., 2007). Given the presence of aqueous Fe(II) in the lateritic environment (e.g., Beukes et al., 2002; Yamaguchi et al., 2007; Wu et al., 2019) and the ubiquity of Sc substitution in goethite in laterites (Ulrich et al., 2019; Qin et al., 2020), it is critical to assess whether or not the adsorbed Sc becomes structurally incorporated into the goethite lattice during Fe(II)-driven goethite recrystallization.

In this study, batch adsorption experiments were performed to investigate the macroscopic adsorption behavior of Sc onto goethite. The effect of aqueous Fe(II) on the adsorption behavior of Sc was also examined. The local coordination environments of Sc in synthetic Sc-adsorbed and Sc-substituted goethite were determined by extended X-ray absorption fine structure (EXAFS) spectroscopy. Quantum chemical calculations were performed to complement EXAFS data interpretation for clarifying the mechanisms of Sc immobilization by goethite at the molecular level. Moreover, the *in situ* speciation and crystal chemistry of Sc in natural goethite particles in the laterite were determined by using micro-focused X-ray fluorescence (μ-XRF), X-ray diffraction (μ-XRD), and μ-XAFS techniques. The aims of this study were to elucidate the molecular-scale mechanisms for Sc adsorption on and structural incorporation into goethite and to provide insights into the geochemical behavior and environmental fates of Sc.

2. MATERIALS AND METHODS

2.1. Materials

Chemical reagents, including $ScCl_3{\cdot}6H_2O$, $Fe(NO_3)_3{\cdot}9H_2O$, and $FeCl_2{\cdot}4H_2O$, were purchased from Wako Pure Chemical Industries, Ltd., Japan. A stock solution of Sc (III) was prepared by dissolving $ScCl_3{\cdot}6H_2O$ in Milli-Q water. The ScOOH gel was obtained by the precipitation of $ScCl_3$ solution under alkaline conditions at room temperature. A stock solution of Fe(II) was prepared from deoxygenated deionized water and $FeCl_2{\cdot}4H_2O$ in an anaerobic chamber (Ar: 95%; H_2: 5%) (Coy Laboratory Products, USA) with low oxygen concentration (<1 ppm).

Pure goethite was synthesized following the procedures proposed by Schwertmann and Cornell (2000). A 90 mL of 5.0 mol/L KOH solution was added rapidly into a bottle containing 50 mL of 1.0 mol/L $Fe(NO_3)_3$ solution and then diluted to 1.0 L with Milli-Q water. After aging for 60 h at 70 °C, the suspension was filtered with a membrane filter (0.20 μm) and washed thoroughly free of electrolytes. The obtained solid phase was freeze-dried for adsorption experiments.

Natural laterite samples were collected from Eramen Ni Mine in Zambales Province of the Philippines, and the geochemical and mineralogical compositions of the samples were investigated in our previous study (Qin et al., 2020). The limonite sample consisting of predominant goethite was selected to prepare the thin section for μ-XRF-XRD-XAFS analysis. Thin section sample was prepared following the procedures previously reported by Qin et al. (2017a). In brief, the sample was embedded in the epoxy resin for 24 h and then double-face polished to a thickness of ~40 μm.

2.2. Batch adsorption experiments

The adsorption of Sc on goethite was investigated using a batch technique under ambient conditions. Goethite, $NaNO_3$ background electrolyte solution, and Sc(III) stock solutions were added into centrifuge tubes. The pH was adjusted to desired values by adding <20 μL of 0.1 M HNO_3 or NaOH solution. Three series of adsorption experiments were conducted at the $NaNO_3$ concentrations of 0.001, 0.010, and 0.10 mol/L with the pH range of 2–10. After equilibration in a shaking water bath at room temperature for 24 h, the suspension was filtered using a disposable syringe (0.20 μm). The adsorption kinetic experiment was performed at pH 5.4 and 0.01 mol/L $NaNO_3$ over a time period of 24 h. The filtrate was diluted adequately to determine Sc concentration by inductively coupled plasma-mass spectrometry (ICP-MS, Agilent 7700). The adsorption percentage ($S\% = (C_0 - C_e)/C_e \times 100\%$) and amount ($q_e = (C_0 - C_e) \times V/m$, mmol/g) of Sc on goethite were calculated from the initial (C_0) and equilibrium (C_e) concentrations of Sc in solution and the solid-to-liquid ratio (m/V, g/L).

The Sc-adsorbed goethite used for XAFS measurement was prepared under pH 5.8 on the basis of our previous investigation of pH values in the Ni laterites from the Philippines (Qin et al., 2020). The solid phase was separated from the final suspension (after 24 h equilibration) with a membrane filter (0.20 μm), and then the solid was rinsed thoroughly with deionized water to remove trace amounts of soluble Sc and packed into a polyethylene bag. Moreover, 1 mmol/L Fe(II) was added into the suspension containing 0.01 mol/L $NaNO_3$ at pH 5.8 and then aged in an anaerobic chamber (Ar: 95%; H_2: 5%; $O_2 < 1$ ppm) for 21 days to investigate the effect of aqueous Fe(II) on Sc adsorption on goethite. The pH was adjusted by adding small amounts of 0.1 M HNO_3 or NaOH solution as needed. The solid product obtained through filtering the suspension was also rinsed thoroughly with deionized water and then packed into a polyethylene bag under anaerobic conditions.

2.3. Desorption experiments

A two-steps desorption experiment was performed for Sc-adsorbed goethite. Specifically, the samples were sequentially extracted using 10.0 mmol/L of CH_3COONH_4 solution and 2.0 mmol/L of EDTA-2Na solution. In general, the CH_3COONH_4 shows an ion-exchange capacity for metal ions, whereas EDTA-2Na has a strong chelating property and can extract ions strongly bound to the adsorbents (Gao et al., 2003; Wu et al., 2018).

2.4. Preparation of Sc-substituted goethite

Sc-substituted goethite was prepared as previously described with some modifications (Chassé et al., 2017). In brief, 5.0 mol/L KOH was added into 100 mL solutions containing appropriate $Fe(NO_3)_3$ and Sc to synthesize Sc-substituted goethite with varying Sc molar proportions ($Sc\% = n_{Sc}/(n_{Sc+Fe}) \times 100$). The suspension was aged at 70 °C for 14 days with occasional shaking. The solid phase was separated by centrifugation, washed at 45 °C for 2 h in a 3.0 mol/L H_2SO_4 solution, and then washed with Milli-Q water for several times to remove possible adsorbed species and any residual Sc-ferrihydrite precursor that may have not been fully converted to goethite.

2.5. Characterization of synthetic materials

The synthetic solid materials, including pure goethite, Sc-adsorbed goethite, and Sc-susbstituted goethite, were characterized using an X-ray diffractometer (RINT-2100, Rigaku) with Cu $K\alpha_1$ ($\lambda = 1.54056$ Å) radiation emitted at 40 kV and 30 mA. The XRD data were recorded in the less-fluorescence mode to minimize the effect of Fe fluorescence on background. The morphology of the samples was observed by scanning electron microscopy (SEM, Hitachi S-4500) at an accelerating voltage of 2 kV.

2.6. Bulk XAFS measurements and data analyses

Bulk Sc K-edge XAFS spectra were recorded at the beamline BL-12C at the Photon Factory, KEK (Tsukuba, Japan) with a Si(111) double-crystal monochromator. The energy of Sc was calibrated using the first peak of Sc_2O_3 at 4.489 keV. The sample was placed at an angle of 45° from the incident beam and determined in fluorescence mode by using a 19-element Ge solid-state detector under ambient conditions. The samples used for bulk Sc K-edge XAFS measurements are listed in Table S1. For comparison with Sc-adsorbed samples, the stock $ScCl_3$ solution with the Sc concentration of 1028 mg/L was also subjected to XAFS measurement. The Sc-substituted goethite-2 (8.5% Sc) was diluted 10 times with BN to avoid possible self-absorption effects because of its high Sc concentration. Based on detailed assessments described in the Supplementary material, the XAFS spectra of the samples examined in this study were unaffected by the self-absorption effects. Several scans were carried out to improve the signal-to-noise ratio of the XAFS spectra.

XANES data were analyzed using REX2000 (Rigaku Co. Ltd.). The background was removed from the raw XANES spectra by a spline smoothing method. Linear combination fittings (LCF) for the XANES spectra were conducted as previously described to obtain Sc speciation quantitatively (Qin et al., 2017b, 2020). For EXAFS analysis, the radial structural function (RSF) was obtained from the Fourier transformation (FT) of the $k^3\chi(k)$ oscillation by using the ATHENA and ARTEMIS software (Ravel and Newville, 2005). Then, the RSF was simulated using the curve-fitting method to obtain structural parameters. The theoretical phase shift and amplitude functions of the Sc-O and Sc-Fe shells for the adsorbed samples were extracted from the structure of $ScFeO_3$ (Kawamoto et al., 2014) by using FEFF 7.02 (Zabinsky et al., 1995). For Sc-substituted goethite, the core Fe atom in the goethite structure model (Gualtieri and Venturelli, 1999) was replaced by Sc atom in the corresponding FEFF file. Details of the EXAFS analysis are similar to those described previously (e.g., Mitsunobu et al., 2010; Qin et al., 2012, 2019).

The quality of the simulation was evaluated by the goodness of fit parameter (R factor), expressed by the following equation:

$$R = \sum \{k^3 x_{obs}(k) - k^3 x_{cal}(k)\}^2 / \sum \{k^3 x_{obs}(k)\}^2 \quad (1)$$

where $\chi_{obs}(k)$ and $\chi_{cal}(k)$ are the experimental and calculated absorption coefficients at a given wavenumber (k), respectively.

2.7. μ-XRF-XRD-XAFS measurements

Micro-focused measurements for the thin section sample were performed at the beamline BL-15A1 at the Photon Factory (Tsukuba, Japan). The thin section sample was spatially scanned to obtain the μ-XRF maps of Sc and Fe. On the basis of the distribution of Sc and Fe, μ-XRD patterns for spots of interest were determined. Meanwhile, the Sc and Fe μ-XAFS spectra of these spots were obtained in fluorescence and transmission modes, respectively.

2.8. Quantum chemical calculations

For density functional theory (DFT) calculations, the geometry of surface complex model was optimized with M06-2X/6-311+G* level (Zhao and Truhlar, 2008) by using the Gaussian 09 program (Frisch et al., 2009). The bidentate-mononuclear (edge-sharing, ^2E) and bidentate-binuclear (cornering-sharing, ^2C) geometries were optimized for Sc adsorption on the goethite surface. In the goethite model, four H_2O molecules were located at the surface to take account of the interaction between Sc and the neighboring OH groups around the binding site (Tanaka et al., 2014, Qin et al., 2019). A seven-fold coordinated complex for hydrated Sc(III) solution was set to compare with the experimental results because the coordination number (CN) of the aqueous $ScCl_3$ solution used in our adsorption experiment is seven (Lindqvist-Reis et al., 2006; Cotton, 2018).

3. RESULTS

3.1. Characterization of synthetic solid materials

The XRD pattern of Sc-substituted goethite was similar to that of the orthorhombic phases of pure goethite (Fig. 1). Despite the absence of additional peaks, the feature peaks of Sc-substituted goethite slightly shifted to lower angles compared with those of pure and Sc-adsorbed goethite (Fig. 1). This observation is in accordance with the peak shift tendency for the continuous solid solution αFeOOH-αScOOH (Levard et al., 2018), strongly suggesting that Sc is incorporated into the goethite structure for the Sc-substituted goethite synthesized in our study.

Fig. 2 shows the morphology of synthetic solid materials by SEM observation. The particles of pure goethite and Sc-adsorbed goethite exhibited a common crystallized acicular structure, consistent with the description on goethite morphology by numerous studies (e.g., Schwertmann and Cornell, 2000; Kosmulski et al., 2004). Interestingly, the acicular particles of Sc-substituted goethite were smaller

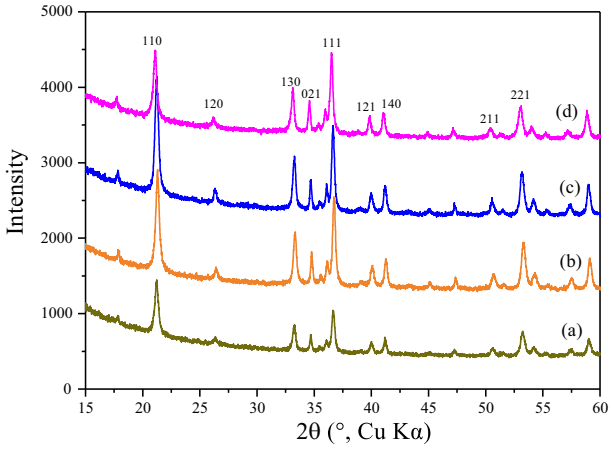

Fig. 1. XRD patterns of synthetic materials (a: pure goethite; b: Sc-adsorbed goethite (no Fe(II), 1d); c: Sc-substituted goethite-1 (1.2% Sc); d: Sc-substituted goethite-2 (8.5% Sc)).

than those of pure goethite, and the width-to-length ratio increased with increasing Sc substitution. In particular, rectangle-like structures were observed for the Sc-substituted goethite-2 with a higher Sc substitution rate (8.5% Sc, Fig. 2d). Levard et al. (2018) also observed via transmission electron microscopy (TEM) that the anisotropy of the formed particles in $Fe_xS_{c(1-x)}OOH$ solid solution decreases with increasing Sc incorporation into the goethite structure. In addition, the lower full width at half maximum (FWHM) values of XRD peaks (e.g., 110) may reflect smaller particle sizes for the goethite with a higher Sc incorporation (Fig. 1d), which is in accordance with the SEM observation (Fig. 2d). Indeed, this correlation between XRD peak and crystal size is particularly clear for the series of continuous (Fe,Sc)OOH solid solution (Levard et al., 2018). The formation of the acicular particles in goethite results from the oriented aggregation of nanoparticles (Domingo et al., 1994; Kosmulski et al., 2004; BurleSon and Penn, 2006). Thus, the incorporation of Sc likely hinders the oriented aggregation of goethite nanoparticles and decreases the crystal size, which is similar to the incorporation of other foreign ions (e.g., Mn and Cr) into the crystal structure of goethite (e.g., Sileo et al., 2004; Liu et al., 2018).

3.2. Macroscopic adsorption results

3.2.1. Adsorption kinetics

The adsorption rate of Sc on goethite was rapid. Approximately 30% of Sc was adsorbed by goethite within the first 10 min, and then the adsorption percentage gradually increased with reaction time and attained an equilibrium after 3 h (Fig. 3). Accordingly, the contact time was set to 24 h in the following adsorption experiments to ensure the attainment of adsorption equilibrium.

The adsorption kinetics data were simulated with the pseudo-first-order (equation (2)) and pseudo-second-order (equation (3)) models as shown below (Ho and McKay, 1999a, 1999b; Ho and Ofomaja, 2006):

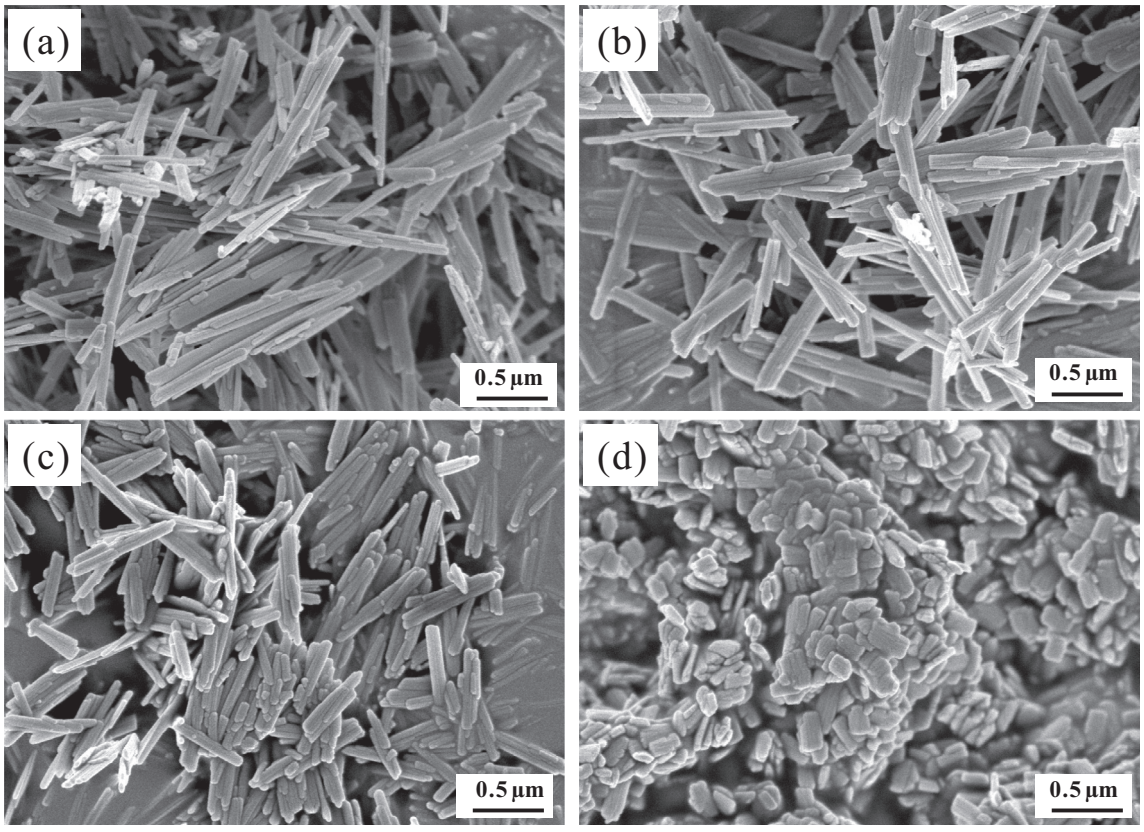

Fig. 2. FE-SEM images of synthetic materials, which were acquired at an accelerating voltage of 2 kV (a: pure goethite; b: Sc-adsorbed goethite (no Fe(II), 1d); c: Sc-substituted goethite-1 (1.2% Sc); d: Sc-substituted goethite-2 (8.5% Sc)).

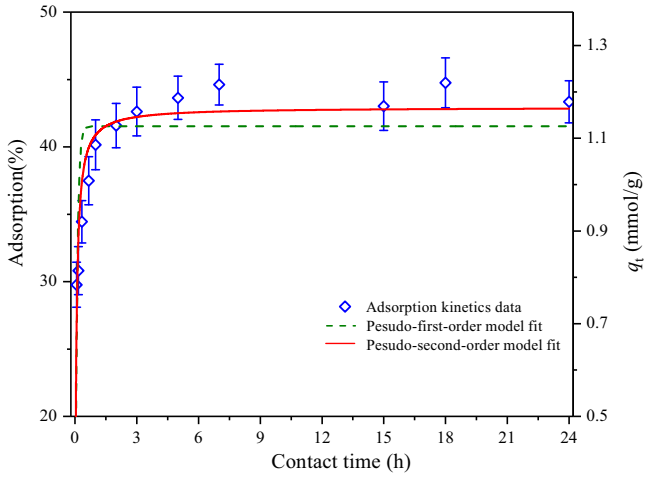

Fig. 3. Kinetics data and corresponding model fits for Sc adsorption on goethite (T = 293 K, pH = 5.4, m/V = 0.1 g/L, C_0 = 10 mg/L, I = 0.01 mol/L $NaNO_3$).

$$q_t = q_{e,cal}\left(1 - e^{-k_1 t}\right) \quad (2)$$

$$q_t = \frac{k_2 t q_{e,cal}^2}{1 + k_2 t q_{e,cal}} \quad (3)$$

where k_1 (h^{-1}) and k_2 (g/(mmol h)) indicate the rate constants of the pseudo-first-order and pseudo-second-order models, respectively; q_t (mmol/g) represents the experimental adsorption amount of Sc by goethite at a specific time (t, h); and $q_{e,cal}$ (mmol/g) is the theoretical adsorption amount predicted by the kinetics model.

The fitting results and kinetic parameters derived from the pseudo-first-order and pseudo-second-order models

are shown in Fig. 3 and Table S2. The kinetic data agreed well with the pseudo-second-order model ($R^2 = 0.979$) compared with the pseudo-first-order model ($R^2 = 0.928$). Moreover, the $q_{e,cal}$ value (1.17 mmol/g) predicted from the pseudo-second-order model was close to the experimental value ($q_{e,exp} = 1.21$ mmol/g). Thus, the better simulation of the pseudo-second-order model on kinetics data suggests that the adsorption of Sc on goethite is predominately derived by chemical binding rather than physical interaction or mass transport (Ho and McKay, 1999a; Wu et al., 2018).

3.2.2. Effects of pH and ionic strength

Fig. 4 illustrates the pH-dependent adsorption trends of Sc on goethite at a series of ionic strength. The adsorption percentage of Sc on goethite was ~10% at pH < 4.0, and then it rapidly increased up to ~100% when the pH was increased to 7.0 and remained ~100% under alkaline conditions (pH > 7.0). These results can be explained by the surface properties of goethite and Sc speciation in solution (Fig. 5) calculated by Visual MINTEQ ver. 3.1 (Gustafsson, 2018). The goethite surface is generally positively charged at pH values below 7.0, as the pH_{pzc} (point of zero charge) of goethite is 5.9–6.7 (Langmuir, 1997). The lower Sc adsorption percentage at low pH (<4.0) is likely due to the strong electrostatic repulsion between goethite and positively charged Sc species in solution (e.g., Sc^{3+}, $Sc(OH)^{2+}$ and $Sc(OH)_2^+$; Fig. 5). In this case, the chemical interaction could play an important role in the adsorption of Sc on goethite. With the increase in pH, Sc was readily adsorbed by the goethite because of the increase in deprotonated surface sites derived from the deprotonation reaction. It should be noted that the ScOOH (*s*) precipitation ($Ksp = 8.0 \times 10^{-31}$) may occur at pH values above 6.4 (Fig. 5). Although we cannot fully exclude the contribution of ScOOH precipitation to Sc sequestration under alkaline conditions, the main immobilization mechanism for Sc by goethite at pH < 6.4 is clearly not ascribed to the precipitation.

Moreover, ionic strength had a negligible influence on the Sc adsorption on goethite within wide pH ranges

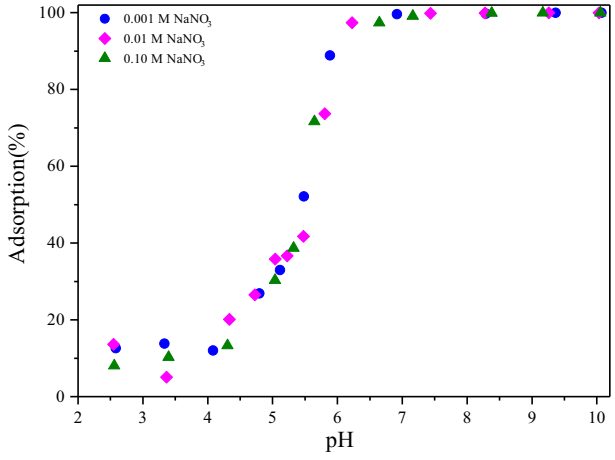

Fig. 4. Effects of pH and ionic strength on the adsorption of Sc on goethite (T = 293 K, m/V = 0.1 g/L, C_0 = 10 mg/L).

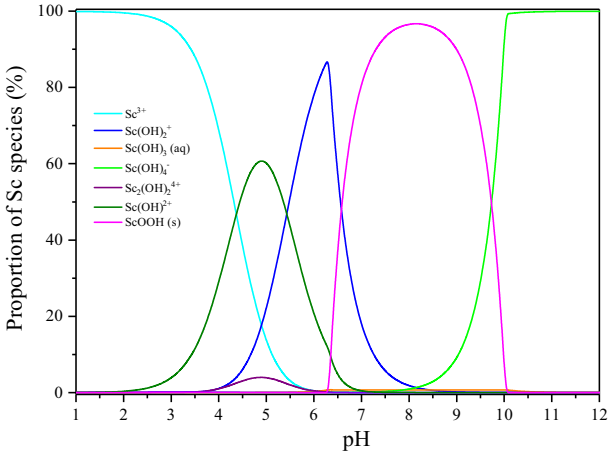

Fig. 5. Chemical speciation of Sc in solution as a function of pH (T = 293 K, C_0 = 10 mg/L, I = 0.01 mol/L $NaNO_3$) calculated by Visual MINTEQ ver. 3.1 (Gustafsson, 2018).

(Fig. 4). This observation excludes the formation of outer-sphere complexes that are ionic strength dependent and indicates the formation of inner-sphere complexes and/or precipitation that are independent of ionic strength (Hayes et al., 1987; Wu et al., 2018).

3.3. Desorption experiments

A small or negligible amount of Sc was detected in the CH_3COONH_4 extract, whereas the majority of Sc (89.1–95.9%) was subsequently desorbed by EDTA-2Na (Table 1). These results could help understand the immobilization mechanism of Sc by goethite. The fraction leached by CH_3COONH_4 represents the outer-sphere complexation because of its good cation exchange capacity, and the EDTA-2Na extraction denotes the uptake mechanism of inner-sphere complexation (Gao et al., 2003; Wu et al., 2018). The residual phase might be related to the precipitation of the insoluble phase (Wu et al., 2018). In the present study, the predominant desorption by EDTA-2Na suggests that Sc is mainly immobilized by goethite with the formation of inner-sphere complexes rather than outer-sphere complexes and precipitation, which is in good agreement with the macroscopic adsorption results.

3.4. Bulk Sc K-edge XAFS analyses

3.4.1. Sc-substituted goethite

As shown in Fig. 6, the Sc K-edge XANES spectra and first derivatives for the Sc-substituted goethite with different Sc substitution rate were essentially identical. Several fingerprint peaks at 4498, 4508, and 4520 eV (marked by red dashed lines) were observed for synthetic Sc-substituted goethite (Fig. 6A(c) and (d)), consistent with the theoretical XANES spectrum restructured by DFT calculations (Chassé et al., 2020). More clearly, two feature peaks appeared at 4496 and 4508 eV (marked by red dashed lines) in the first derivative of Sc-substituted goethite (Fig. 6B), which can be used to distinguish adsorbed and substituted species in solid samples.

Table 1
Desorption percentages of Sc from the uptake samples by using CH_3COONH_4 and EDTA-2Na as the extractants.

Experimental conditions	Sorption amount (mmol/g)	Desorption* by CH_3COONH_4 (%)	Desorption* by EDTA-2Na (%)
pH = 4.1	0.54	0.002	94.4
pH = 5.4	1.21	0.017	91.7
pH = 5.8	1.99	0.065	89.1
pH = 7.0	2.58	0.003	95.9
pH = 9.8	2.70	0.059	89.4

* Desorption percentage was calculated by referring to the sorption amount of Sc.

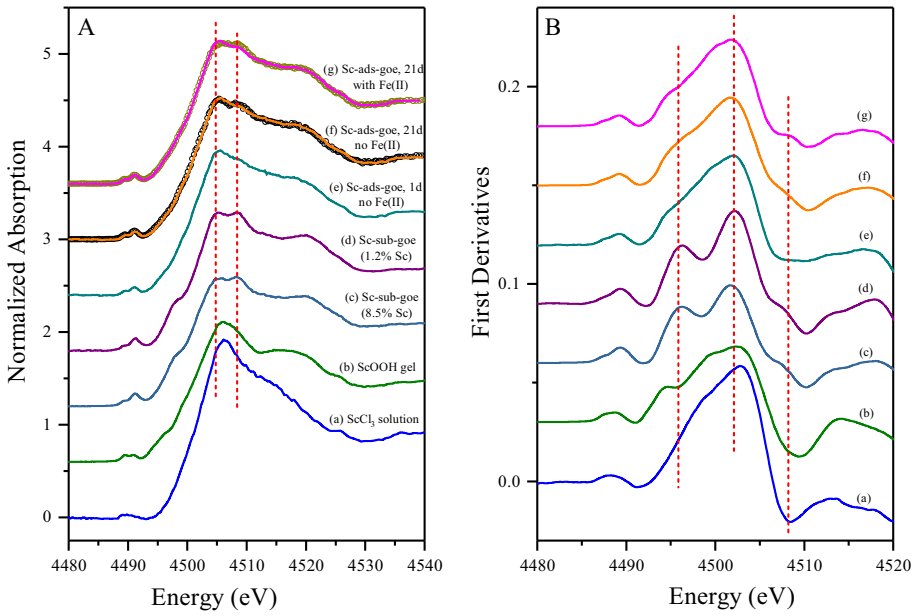

Fig. 6. Sc K-edge XANES spectra (A) and first derivatives (B) for synthetic materials. For the samples (f) and (g), dotted lines are spectra obtained by experiments, and solid lines are calculated spectra by the LCF analysis.

The $k^3\chi(k)$ spectra of Sc K-edge EXAFS and their RSFs (phase shift not corrected) of the samples are illustrated in Fig. 7A and B, respectively. Sc-substituted goethite exhibited two apparent bulges around 7.0–9.0 $Å^{-1}$ in the $k^3\chi(k)$ spectra (Fig. 7A(c) and (d)) and strong second peaks at R + ΔR = 2.3–3.5 Å (phase shift not corrected) in the RSFs (Fig. 7B(c) and (d)), which can be ascribed to considerable backscattering signals from the surrounding Fe atoms. In specific, the peaks around 5.5, 7.5, and 8.5 $Å^{-1}$ in the k space of Sc-substituted goethite overlapped with the maximum of the inversely Fourier-filtered Sc-Fe waves (Fig. S1), which clearly indicates the contribution of three Sc-Fe shells. Quantitative analysis for the RSFs of Sc-substituted goethite by the curve-fitting method showed that the interatomic distances between Sc and Fe atoms were 3.12–3.13, 3.36, and 3.53 Å for the three Sc-Fe shells, whereas the first prominent peaks around R + ΔR = 1.6 Å (phase shift not corrected) were assigned to two Sc-O shells at 2.05–2.06 and 2.17 Å (Table 2).

3.4.2. Sc-adsorbed goethite

The XANES and EXAFS spectra of the Sc-adsorbed goethite prepared at pH 5.8 for 1d were significantly different from those of $ScCl_3$ solution, ScOOH gel, and Sc-substituted goethite (Figs. 6 and 7). These observations suggest that neither outer-sphere complexation nor precipitation is the main sequestration mechanism for Sc adsorption on goethite. Interestingly, the distant peak around R + ΔR = 2.8–3.6 Å (phase shift not corrected) was apparently observed in the RSF of Sc-adsorbed goethite (no Fe(II), 1d) apart from the prominent peak around R + ΔR = 1.6 Å (phase shift not corrected), pointing to the contribution of high Sc-Fe backscattering paths (Fig. 7B(e)). The $k^3\chi(k)$ spectrum of this Sc-adsorbed goethite can be well reconstructed by the inversely Fourier-filtered Sc-O and Sc-Fe shell (Fig. S2). The presence of the second Sc-Fe shell indicates that Sc is adsorbed on goethite with the formation of inner-sphere complexes.

The structural parameters of $ScCl_3$ solution, ScOOH gel, and Sc-adsorbed goethite obtained from the curve-fitting analysis are summarized in Table 3. The pronounced peak in the RSF of aqueous $ScCl_3$ solution was assigned to approximately seven O atoms at a distance of 2.16 Å from the central Sc atom, which is comparable to that of Sc(III) hydration geometry reported previously (e.g., Lindqvist-Reis et al., 2006; Cotton, 2018). In the case of ScOOH gel, the fitted distances for the Sc-O and Sc-Sc bonds were 2.10 and 3.27 Å, respectively. As for Sc-adsorbed goethite

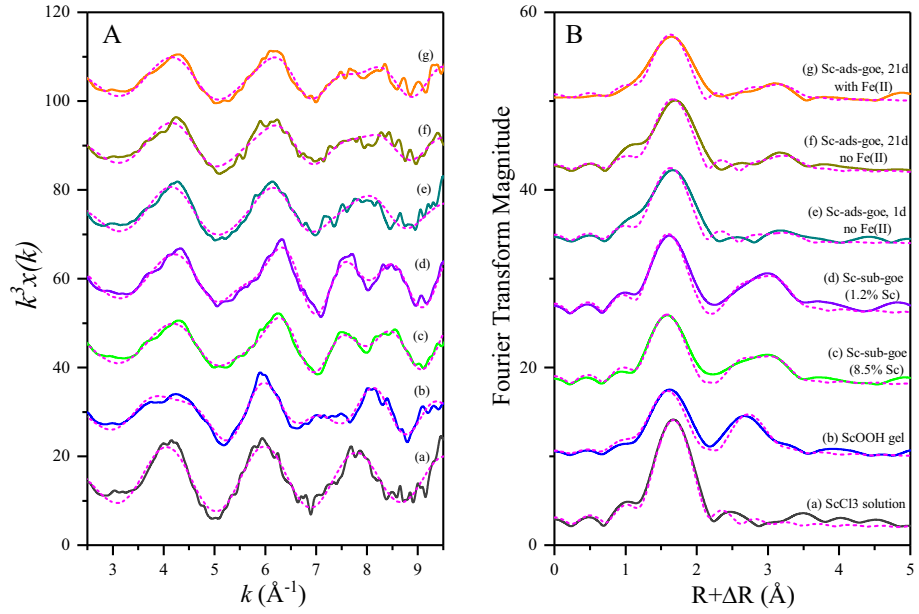

Fig. 7. Sc K-edge EXAFS spectra for synthetic materials (A: k^3-weighted $x(k)$ spectra; B: RSFs (phase shift not corrected)). Solid lines are spectra obtained by experiments, and red dash lines are calculated spectra by a curve-fitting analysis. (For interpretation of the references to colour in this figure legend, the reader is referred to the web version of this article.)

Table 2
Structural parameters of Sc-substituted goethite obtained by a curve-fitting analysis of Sc K-edge EXAFS spectra.

Sample	Shell	CN[a]	R (Å)	ΔE_0 (eV)	σ^2 (Å^2)	χ^2_ν	*R* factor
Sc-substituted goethite-1	Sc-O_1	3	2.06(4)[b]	1(2)	0.001[c]	162	0.019
(1.2% Sc)	Sc-O_2	3	2.17(4)		0.001(2)		
	Sc-Fe_1	2	3.12(6)		0.002(3)		
	Sc-Fe_2	2	3.36(8)		0.003		
	Sc-Fe_3	4	3.53(8)		0.007(6)		
Sc-substituted goethite-2	Sc-O_1	3	2.05(4)	−1(2)	0.001[c]	198	0.021
(8.5% Sc)	Sc-O_2	3	2.17(3)		0.001(2)		
	Sc-Fe_1	2	3.13(4)		0.002(3)		
	Sc-Fe_2	2	3.36(9)		0.003		
	Sc-Fe_3	4	3.53(6)		0.009(6)		

CN: coordination number; R: interatomic distance; ΔE_0: threshold E_0 shift; σ^2: Debye-Waller factor; χ^2_ν: reduced chi-square value; S_0^2: amplitude reduction factor, 0.85, estimated by the fitting for Sc_2O_3 standard.

[a] Fixed the CN to crystallographic values during the analyses.

[b] The uncertainties in the last digit for R, ΔE_0, and σ^2 are reported in parentheses. Parameters with no listed uncertainties were not varied in the analyses.

[c] Constrained to the same value for the two Sc-O shells during the analyses.

(no Fe(II), 1d), the first peak was composed of nearly six O atoms at 2.13 Å, and the distant peak following the Sc–O shell corresponded to the Sc–Fe shell with the interatomic distance of 3.61 Å (Table 3).

3.4.3. Effect of aqueous Fe(II) on Sc adsorption on goethite

For the Sc-adsorbed goethite prepared in the presence of aqueous Fe(II), the appearance of another feature peak at 4508 eV in the XANES spectrum (Fig. 6A(g)) clearly indicates the formation of Sc-substitute species. This observation is also confirmed by the presence of a small feature peak at 4508 eV in the first derivative of the sample (Fig. 6B(g)). With Sc-substituted goethite-1 (1.2% Sc) and Sc-adsorbed goethite (no Fe(II), 1d) as the end members, the LCF result showed that as much as 26% of adsorbed Sc was incorporated into the goethite structure in the presence of aqueous Fe(II) after the aging of 21 days (Fig. 6A (g) and Table 4). By contrast, much less incorporation (5%) was observed for the sample prepared in the absence of Fe(II), even after 21 days (Fig. 6A(f) and Table 4). The LCF analysis of EXAFS presented similar speciation results with the XANES assessments, albeit elevated noise in the EXAFS spectra (Fig. S3). In general, XANES reflects the valence and symmetry of the element, whereas EXAFS reflects the information of neighboring atoms, interatomic distances, and coordination numbers. Thus, the consistency

Table 3
Structural parameters of Sc-adsorbed goethite and reference materials obtained by a curve-fitting analysis of Sc K-edge EXAFS spectra.

Sample	Shell	CN	R (Å)	ΔE_0 (eV)	σ^2 (Å^2)	χ^2_v	*R* factor
$ScCl_3$ solution	Sc-O	6.8(1.5)[a]	2.16(2)[b]	−1(2)[b]	0.003(2)[b]	50	0.041
ScOOH gel	Sc-O	6.0(1.1)	2.10(2)	−7(2)	0.006(2)	152	0.054
	Sc-Sc	2.8(1.3)	3.27(3)		0.003		
Sc-adsorbed goethite	Sc-O	6.1(1.5)	2.13(2)	−1(2)	0.005(3)	116	0.061
(no Fe(II), 1 d)	Sc-Fe	1.4(1.8)	3.61(6)		0.009		
Sc-adsorbed goethite	Sc-O	5.8(1.5)	2.15(2)	1(2)	0.005(3)	97	0.067
(no Fe(II), 21 d)	Sc-Fe	1.6(0.8)	3.60(5)		0.005		
Sc-adsorbed goethite	Sc-O	5.6(1.3)	2.13(2)	−2(2)	0.006(3)	108	0.058
(with Fe(II), 21 d)	Sc-Fe	2.3(1.1)	3.56(5)		0.009		

CN: coordination number; R: interatomic distance; ΔE_0: threshold E_0 shift; σ^2: Debye-Waller factor; χ^2_v: reduced chi-square value; S_0^2: amplitude reduction factor, 0.85.
[a] The uncertainties of the CN are listed in parentheses. Parameters with no listed uncertainties were not varied in the analyses.
[b] The uncertainties in the last digit for R, ΔE_0, and σ^2 are reported in parentheses.

Table 4
Sc speciation in studied samples by linear combination fitting (LCF) of Sc K-edge XANES spectra.

Sample	Sc-ads-goe (%)	Sc-sub-goe (%)	Sum (%)[b]	*R* factor (%)
Sc-adsorbed goethite (no Fe(II), 21 d)	94(2)[a]	6(2)	100.1	0.015
Sc-adsorbed goethite (with Fe(II), 21 d)	75(4)	26(4)	101.4	0.013
Spot 1	22(5)	77(5)	99.2	0.036
Spot 2	35(7)	66(7)	101.2	0.034

Sc-ads-goe: Sc-adsorbed goethite (no Fe(II), 1 d); Sc-sub-goe: Sc-substituted goethite-1 (1.2% Sc).
[a] The uncertainties in the last digit are reported in parentheses.
[b] The sum of the fitting component by the LCF analysis.

between the LCF results of XANES and EXAFS strongly suggests that Sc speciation estimated in our study is highly reliable and robust.

Furthermore, the curving-fitting results of the sample prepared in the presence of aqueous Fe(II) showed different structural parameters for the Sc-Fe shell, with a slightly shorter distance (3.56 Å) and a larger CN (2.3) in contrast to those of the samples without Fe(II) influence ($R_{Sc\text{-}Fe}$ = 3.60–3.61 Å and CN = 1.4–1.6, Table 3). This difference can be attributed to the partial incorporation of Sc into the goethite structure, considering that Sc-substituted goethite exhibits significant Fe backscattering signals (Fig. 7 and Table 2). Thus, we demonstrate that Sc adsorbed on the goethite surface can be progressively incorporated into the goethite structure in the presence of aqueous Fe(II).

3.5. Micro-focused analyses of natural goethite

3.5.1. μ-XRD and Fe K-edge μ-XAFS

On the basis of the μ-XRF mapping of Sc and Fe, two particles enriched with Fe and Sc (indicated with circles in Fig. 8A) were selected to perform μ-XRD and μ-XAFS measurements. The μ-XRD patterns of the two particles were similar, and goethite was identified from the diffraction peaks to be the predominant mineral (Fig. 8B).

To further distinguish the presence of poorly-crystalline ferrihydrite that is hardly identified by XRD analysis, we also collected the Fe K-edge μ-XAFS spectra of the two spots. Their peak positions and features in the pre-edge and post-edge regions of the μ-XANES spectra were essentially identical to those of goethite (Fig. 8C). Moreover, the good match between the frequencies and amplitudes of the μ-EXAFS spectra was observed for the two particles and goethite (Fig. 8D). The further LCF analysis with ferrihydrite and goethite as the end members showed that Fe is predominantly present as goethite (91–94%) along with a small amount of ferrihydrite (<9%, Fig. S4), which confirms the identification of natural goethite particles by μ-XRD and Fe μ-XANES analyses.

3.5.2. Sc K-edge μ-XAFS

We carried out *in situ* Sc K-edge μ-XAFS measurements for the two identified goethite particles to investigate the speciation and local environment of Sc in natural goethite. The natural goethite examined here exhibited distinguishable XANES features with Sc-substituted goethite, particularly for the presence of two feature peaks at 4496 and 4508 eV in the first derivatives (Fig. 9B). By LCF analysis of μ-XANES spectra, Sc speciation in natural goethite is dominated by the species incorporated into the crystal structure (69–79%) along with a small amount of adsorbed Sc (21–31%) on the goethite surface (Fig. 9A and Table 4).

In the present study, the high Sc contents in the goethite particles allowed us to first collect Sc K-edge μ-EXAFS spectra in natural samples. Despite the relatively poor quality, the $k^3\chi(k)$ spectra of natural goethite were more analogous to those of Sc-substituted goethite (Fig. 10). Further

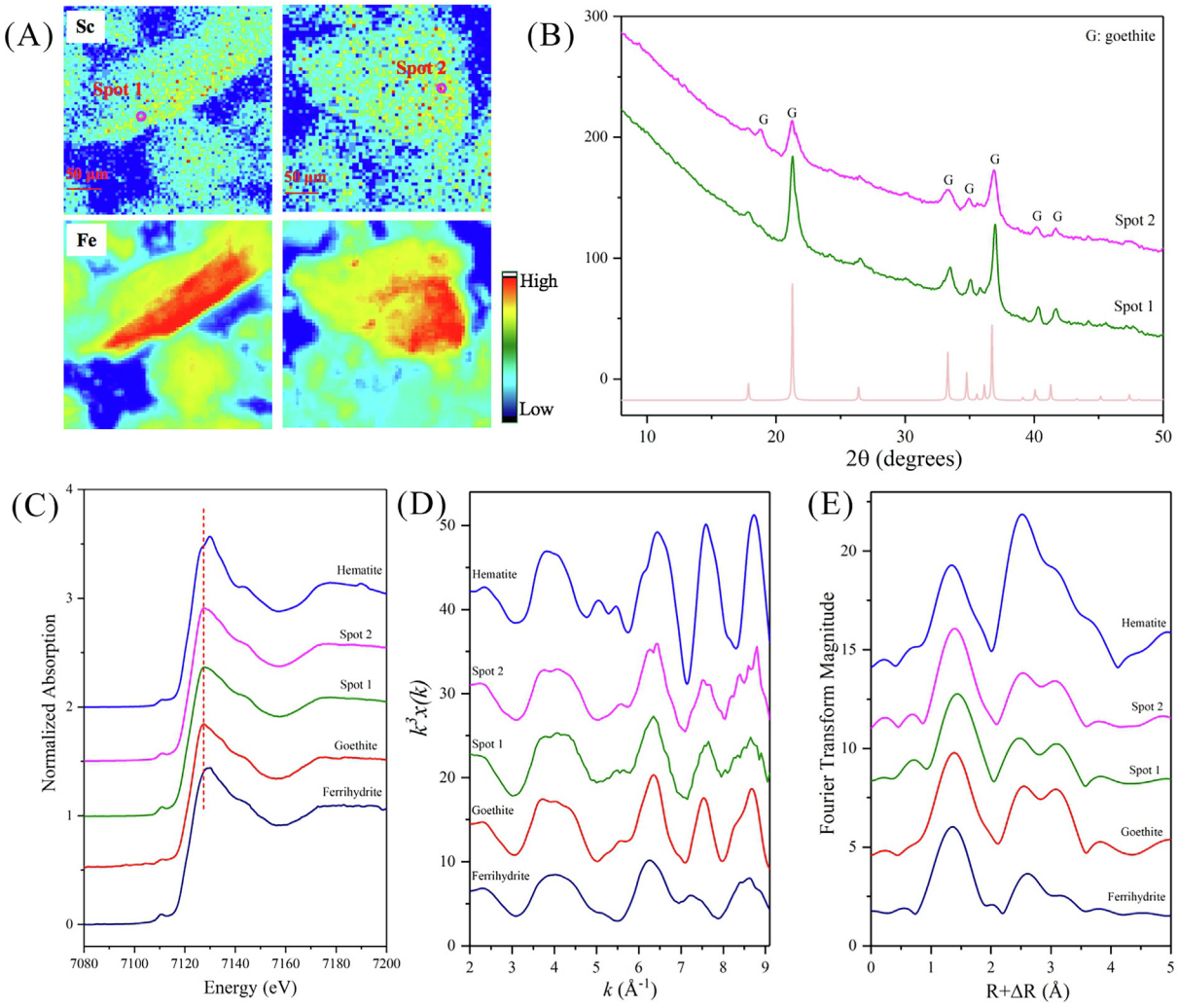

Fig. 8. Micro-focused analyses for the identification of natural goethite particles (A: μ-XRF maps showing the elemental distribution in natural laterite. The open circles in the map of Sc indicate the spots of interest for further μ-XRD, Sc and Fe K-edge μ-XAFS measurements. The results of μ-XRD patterns, Fe K-edge μ-XANES, k^3-weighted $x(k)$ spectra, and RSFs (phase shift not corrected) of the two particles are shown in B, C, D, and E, respectively).

LCF analysis of these μ-EXAFS spectra also showed higher percentages of Sc substitution species in the two goethite particles (Fig. S3), which is consistent with the speciation results derived from the μ-XANES fitting (Table 4). Moreover, the curve-fitting analysis indicated that the pronounced peak is composed of two Sc-O shells with bond lengths of 2.07–2.08 and 2.17–2.19 Å (Table 5). Similar to synthetic Sc-substituted goethite, the next-nearest-neighbor shell at R + ΔR = 2.5–3.5 Å (phase shift not corrected) could be rationally fitted by the three Sc-Fe shells model, in which the interatomic distances between Sc and Fe atoms were 3.15–3.17, 3.43, and 3.65–3.66 Å (Table 5).

3.6. DFT calculations

According to DFT calculations, the theoretical Sc-Fe distances for the bidentate–binuclear (corner-sharing, ^2C) complex and bidentate–mononuclear (edge-sharing, ^2E) complex were 3.61 and 3.04 Å, respectively, whereas the average Sc-O bond length for both complexes was 2.20 Å (Fig. 11). These Sc-O and Sc-Fe bond lengths in the bidentate–binuclear complex obtained from DFT calculations are highly comparable to those derived from the EXAFS analysis of Sc-adsorbed goethite ($R_{Sc\text{-}O} = 2.13$ Å and $R_{Sc\text{-}Fe} = 3.61$ Å, Table 3). This consistency suggests that Sc is predominantly adsorbed on goethite via the bidentate–binuclear corner-sharing complexation.

4. DISCUSSION

4.1. Molecular mechanisms for Sc adsorption on goethite

A number of studies have explored the mechanisms underlying the adsorption of metal(liod)s on minerals through surface complex modeling, quantum chemical calculations, and EXAFS analyses (e.g., Randall et al., 1999; Catalano et al., 2008; Sherman et al., 2008; Qin et al., 2012, 2019; Villalobos et al., 2014). However, the

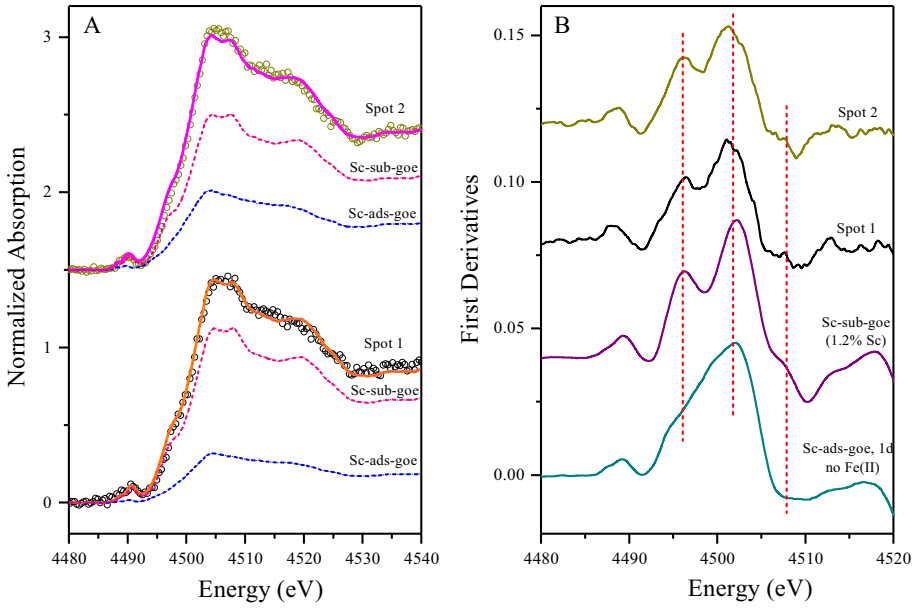

Fig. 9. Sc K-edge μ-XANES spectra (A) and first derivatives (B) for the two natural goethite particles. Dotted lines are spectra obtained by experiments, and solid lines are calculated spectra by the LCF analysis. Blue and red dash lines represent the contribution of Sc-adsorbed goethite (no Fe(II), 1d) and Sc-substituted goethite (1.2% Sc) to the fitted spectra. (For interpretation of the references to colour in this figure legend, the reader is referred to the web version of this article.)

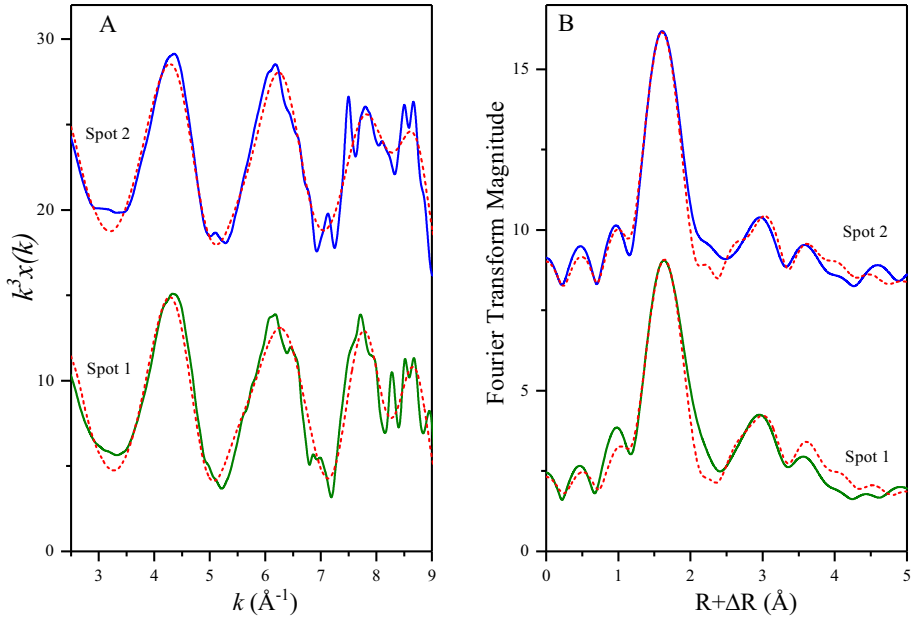

Fig. 10. Sc K-edge μ-EXAFS spectra for the two natural goethite particles (A: k^3-weighted $x(k)$ spectra; B: RSFs (phase shift not corrected)). Solid lines are spectra obtained by experiments, and red dash lines are calculated spectra by a curve-fitting analysis. (For interpretation of the references to colour in this figure legend, the reader is referred to the web version of this article.)

adsorption behavior and molecular-scale mechanisms for Sc sequestration by goethite remain unclear. In this study, in combination with the ionic-strength-independent adsorption trend (Fig. 4) and the great Sc desorption by the EDTA-2Na ligand (Table 1) in macroscopic experiments, the presence of the Sc-Fe shell in Sc-adsorbed goethite from EXAFS analysis (Fig. 7 and Table 3) clearly demonstrated that the inner-sphere complexation is the predominant retention mechanism for Sc adsorption on goethite.

In general, metal(loid)s are adsorbed on iron (oxyhydr) oxides with the binding modes of either inner-sphere or outer-sphere complexation, which could be systematically predicted by their proton dissociation constant (p*K*a) of conjugate acids for anions and their stability constant

Table 5
Structural parameters of natural goethite particles obtained by a curve-fitting analysis of Sc K-edge EXAFS spectra.

Sample	Shell	CN	R (Å)	ΔE_0 (eV)	σ^2 (Å^2)	χ^2_v	*R* factor
Spot 1	Sc-O_1	3	2.07(4)[b]	2(3)[b]	0.004[c]	292	0.054
	Sc-O_2	3	2.19(3)		0.004(3)		
	Sc-Fe_1	0.8(0.6)[a]	3.15(5)		0.002(3)		
	Sc-Fe_2	2.5(1.2)	3.43(7)		0.002		
	Sc-Fe_3	2.8(2.2)	3.65(8)		0.008		
Spot 2	Sc-O_1	3	2.08(4)	3(3)	0.004[c]	266	0.039
	Sc-O_2	3	2.17(4)		0.004(3)		
	Sc-Fe_1	0.8(0.5)	3.17(5)		0.002(2)		
	Sc-Fe_2	2.2(0.9)	3.43(5)		0.002		
	Sc-Fe_3	2.4(2.0)	3.66(8)		0.008		

CN: coordination number; R: interatomic distance; ΔE_0: threshold E_0 shift; σ^2: Debye-Waller factor; χ^2_v: reduced chi-square value; S_0^2: amplitude reduction factor, 0.85.
[a] The uncertainties of the CN are listed in parentheses. Parameters with no listed uncertainties were not varied in the analyses.
[b] The uncertainties in the last digit for R, ΔE_0, and σ^2 are reported in parentheses.
[c] Constrained to the same value for the two Sc-O shells during the analyses.

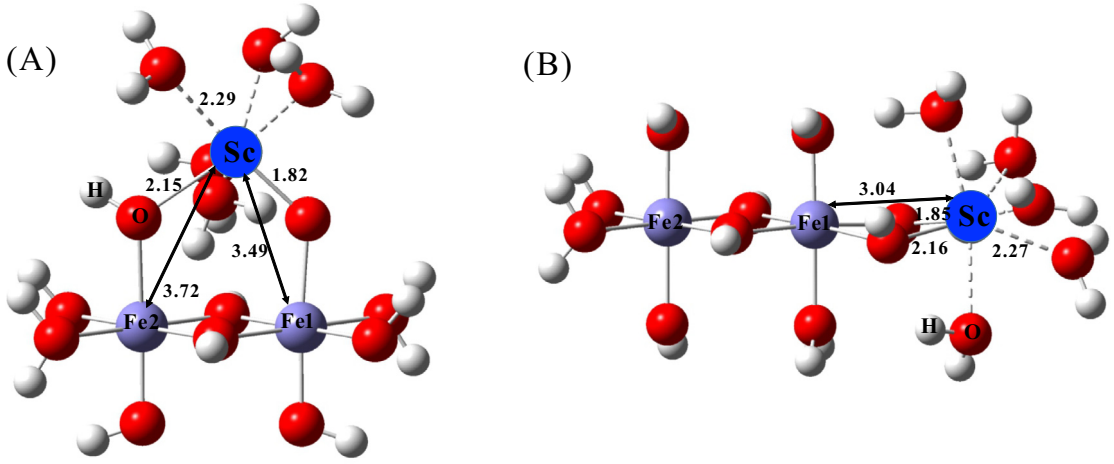

Fig. 11. Optimized structures of surface complexes for Sc adsorbed on goethite (A: bidentate-binuclear complex; B: bidentate-mononuclear complex; red = O, white = H, violet = Fe, blue = Sc; bond lengths shown in Å). (For interpretation of the references to colour in this figure legend, the reader is referred to the web version of this article.)

($\log\beta_{OH}$) with hydroxide for cations (Takahashi et al., 2015; Qin et al., 2017a). Cations with large $\log\beta_{OH}$ values (e.g., Cd^{2+} and Cu^{2+}) exhibit a high affinity for iron (oxyhydr) oxides and tend to form inner-sphere complexes, which may be related to the linear free energy relationship (LFER) (Dzombak and Morel, 1990; Takahashi et al., 2015). According to this systematics trend for the binding modes of metal cations, Sc could be preferentially adsorbed on iron (oxyhydr)oxides via the inner-sphere complexation due to the larger $\log\beta_{OH}$ value and higher ionic potential for Sc^{3+}, which is consistent with our finding regarding the adsorption mechanism for Sc on goethite.

To help verify the structural models of the formed Sc complexes on goethite, we optimized the geometries for clusters analogous to bidentate edge-sharing (^2E) and corner-sharing (^2C) surface complexes by using DFT calculations (Fig. 11). The consistency between DFT calculations and EXAFS results about Sc-O and Sc-Fe bond lengths (Fig. 11 and Table 3) strongly suggests that Sc is preferentially adsorbed on goethite with the formation of bidentate surface complexes at corner-sharing sites on the predominant {110} face of goethite via the O atoms bound to adjacent Fe atoms. Similar immobilization mechanisms have also been found for the adsorption of other metal(loid)s (e.g., Cd, As, V, and U) to goethite (e.g., Randall et al., 1999; Sherman and Randall, 2003; Peacock and Sherman, 2004; Sherman et al., 2008). By contrast, the formation of bidentate–mononuclear complexes (^2E) with a short Sc–Fe distance (3.04 Å) could be very small or negligible because the ^2E complex is energetically unfavorable and only forms on the edge-sharing sites in the {001} and {021} faces that usually comprise a very small fraction of the total goethite surface (Randall et al., 1999; Boily et al., 2001; Peacock and Sherman, 2004).

4.2. Structural incorporation of Sc into goethite

Many foreign ions (e.g., Ni^{2+}, Al^{3+}, Cr^{3+}, Ga^{3+}, Co^{3+}, Sb^{5+}, and Te^{6+}) can substitute for Fe(III) in the crystal structure of goethite, and the extent of incorporation is

largely governed by their ionic radius, valences, and bonding natures (e.g., Manceau et al., 2000; Carvalho-e-Silva et al., 2003; Sileo et al., 2004; Mitsunobu et al., 2010; Kashiwabara et al., 2014; Liu et al., 2018). As for Sc(III), a continuous $Fe_xSc_{(1-x)}OOH$ solid solution has been recently synthesized in the laboratory by Levard et al. (2018). They theoretically explained this phenomenon as follows: (i) the difference (13.4%) in ionic radius between Sc(III) (0.745 Å) and Fe(III) (0.645 Å) is less than the threshold value (15%) for continuous solid solutions stipulated by the first Goldschmidt's rule and (ii) the difference (4%) between the Sc-O and Fe-O bond lengths is also less than the threshold value (5%) in the lattice parameter that makes the Vegard's law valid for ideal solid solutions (Jacob et al., 2007; Levard et al., 2018).

The present study is the first to report coordination environments of Sc in Sc-substituted goethite by EXAFS analysis. EXAFS results indicated that the central Sc atom in Sc-substituted goethite was surrounded by two types of O atoms ($R_{Sc-O1} = 2.06$ Å and $R_{Sc-O2} = 2.17$ Å, Table 2). The DFT calculations by Chassé et al. (2020) showed that the distances of six Sc-O bonds in the goethite with a low amount of Sc incorporation are 2.03, 2.07, 2.07, 2.16, 2.16, and 2.15 Å, respectively, which agree with our EXAFS results. The EXAFS and DFT results consistently suggest the isomorphous substitution of Sc(III) for Fe(III) within the goethite structure. The slight change in Sc-O distances relative to Fe-O distances further indicates that the structure of goethite accommodates Sc substitution without a significant change in the cell volume at a low rate of Sc substitution (Chassé et al., 2020). However, it could be expected that the variation in lattice parameters will be larger at a higher rate of Sc substitution. Indeed, based on the Rietveld refinement of XRD data for a series of (Fe,Sc)OOH samples, Levard et al. (2018) demonstrated that the changes in cell parameters and in the associated cell volume as a function of the substitution rate of Fe by Sc are almost perfectly linear for all parameters and follow Vegard's law.

For the next-nearest-neighbor Sc-Fe shell, the best fit can be obtained by a three-shell model because goethite possesses two edge-sharing links of Fe-Fe (EC and EC′) and one double corner-sharing link of Fe-Fe (DC) in the structure (Gualtieri and Venturelli, 1999). The $Sc\text{-}Fe_1$ shell at 3.12–3.13 Å and the $Sc\text{-}Fe_2$ shell at 3.36 Å for Sc-substituted goethite could correspond to two adjacent octahedra in the chains (EC) and in the row (EC′) for pure goethite, respectively, whereas the $Sc\text{-}Fe_3$ shell ($R_{Sc-Fe3} = 3.53$ Å) corresponds to the double corner-sharing link (DC) in the structure. Nevertheless, these Sc-Fe distances in Sc-substituted goethite are greater than the corresponding Fe-Fe bond lengths in pure goethite (EC: 3.01 Å, EC′: 3.28 Å and DC: 3.46 Å) (Gualtieri and Venturelli, 1999), which is likely attributed to the distortion of the crystal structure of goethite. For the substitution of other metals (M) (e.g., Ni^{2+}, Sb^{5+} and Cr^{3+}) into the goethite structure, similar differences have also been found between M-Fe and Fe-Fe distances (e.g., Carvalho-e-Silva et al., 2003; Sileo et al., 2004; Mitsunobu et al., 2010). The EXAFS results regarding the distortion of the goethite structure are also supported by the shift of diffraction peaks for Sc-substituted goethite from the XRD observations in our study and Levard et al. (2018). The differences in ionic radius and charge between foreign metals and Fe(III) in goethite could result in the change in *d*-spacing and distortion of the structure once the substitution occurs (Mitsunobu et al., 2010; Levard et al., 2018; Liu et al., 2018).

Most importantly, the present study provides *in situ* spectroscopic evidence for the structural incorporation of Sc into natural goethite, revealing that Sc(III) substitution for Fe(III) within goethite is a critical geochemical process for Sc immobilization. Despite good matches in the XANES and EXAFS spectra, the intensity of the distant Sc-Fe peaks for natural goethite was lower than those for synthetic Sc-substituted goethite (Fig. 10). This disparity could be explained by several reasons. First, the disorder of Sc local structure may be larger for natural goethite with the fine-grained nature, resulting in weaker Sc-Fe peaks in natural goethite. This is supported by the Fe K-edge EXAFS result that much weaker distant shell (Fe-Fe) beyond the prominent Fe-O peak is observed in natural goethite than in synthetic goethite because of the higher disorder for natural goethite (Fig. 8E). Second, the Fe backscattering signals of natural goethite could be affected by the presence of adsorbed Sc species (21–31%) to some extent. The larger Sc-Fe bond lengths and lower CNs in natural goethite than those in synthetic Sc-substituted goethite (Table 5) may partly reflect the contribution of adsorbed Sc species, considering that the Sc-Fe shell in Sc-adsorbed goethite had a relatively longer interatomic distance but a lower CN compared with Sc-substituted goethite (Tables 2 and 3). Third, the incorporation of Sc into natural goethite in the laterite may be influenced by the competition from other coexisting cations that are capable of substituting for Fe(III) in goethite, such as Al^{3+}, Co^{3+}, Cr^{3+}, and Ni^{2+}. For example, previous studies have reported the preference of Co over Al, Cd over Al, and Mn over Al for the substitution for Fe(III) in goethite (e.g., Alvarez et al., 2007; Yin et al., 2020). Therefore, in combination with previous studies about Sc substitution into the goethite structure by XRD analysis (Levard et al., 2018) and DFT calculations (Chassé et al., 2020), the findings of our study obtained by EXAFS analysis provide direct atomic-scale information for the structural incorporation of a few Sc into goethite, thereby improving our understanding of Sc immobilization in natural environment.

4.3. Possible controlling factor for Sc speciation in the environment: The role of aqueous Fe(II)

Sc is mostly associated with (oxyhydr)oxides in a variety of environments, such as laterites, soils, and bauxites (e.g., Poledniok, 2008; Chassé et al., 2017, 2019; Vind et al., 2018; Teitler et al., 2019; Ulrich et al., 2019). Poledniok (2008) reported that Sc in Upper Silesia soil is mainly present in the Fe-Mn oxide fraction by sequential extractions. Chassé et al. (2017) found that Sc adsorbed on goethite accounts for 80% of total Sc in the laterites from the

Syerston-Flemington deposits in Australia. Nonetheless, several recent studies proposed that Sc could be mainly incorporated into the goethite structure in Ni laterites from New Caledonia and the Philippines (Muñoz et al., 2017; Ulrich et al., 2019; Qin et al., 2020). These limited but incongruent studies on Sc speciation in natural samples suggest that Sc can be sequestrated by goethite via adsorption, incorporation, or the mixing of the both mechanisms. However, the factor controlling the Sc speciation in the environment is still largely unknown.

In this study, we demonstrate the significant effect of aqueous Fe(II) on Sc speciation in goethite by Sc K-edge XAFS analysis. In specific, the adsorbed Sc on the goethite surface can be incorporated into the crystal structure to a large degree in the presence of aqueous Fe(II), which is likely due to goethite recrystallization induced by aqueous Fe(II). Previous researches have clearly observed that goethite recrystallization can be rapidly activated by aqueous Fe(II) because of the exchange of extensive Fe atoms between solid mineral and solution (Yanina and Rosso, 2008; Handler et al., 2009, 2014; Frierdich et al., 2014; Gorski and Fantle, 2017; Taylor et al., 2019). This Fe(II)-catalyzed recrystallization possibly involves Fe(II) sorption, electron transfer between adsorbed Fe(II) and lattice Fe (III), and conduction of injected electrons to different Fe (III) lattice sites, which then undergo reductive release as Fe(II) (Handler et al., 2009, 2014; Taylor et al., 2019). The extent of atom exchange may be thermodynamically driven by the "healing" of defects at the goethite surface (Notini et al., 2018; Taylor et al., 2019). During goethite recrystallization, the adsorbed Sc(III) near the regions undergoing localized Fe(II) oxidative growth can become progressively overgrown and incorporated into the structural sites of goethite (Fig. 12). Similarly, Fe(II)-catalyzed recrystallization can lead to the progressive incorporation of adsorbed Ni(II) and Sb(V) into the goethite structure (Frierdich et al., 2011; Burton et al., 2020).

In general, goethite recrystallization occurs slowly under oxidizing conditions, but the reductive dissolution of the goethite in lateritic, sedimentary, and soil environments would be activated by the aqueous Fe(II) generated by abiotic and microbial iron reduction under reducing conditions (Frierdich et al., 2011, 2019a; Weber et al., 2006; Crosby et al., 2007). Recent studies have suggested that aqueous Fe(II)-activated goethite recrystallization could result in the redistribution of trace elements (e.g., Ni and Sb) between surface adsorption and the interior of the mineral (e.g., Frierdich et al., 2011, 2019a; Burton et al., 2020). Accordingly, we propose here that the incorporation of Sc into the goethite lattice could be controlled by the dynamic recrystallization of goethite promoted by aqueous Fe(II). The partitioning and speciation of Sc in goethite may reflect the extent of past Fe(II)-Fe(III) cycling in the environments that have undergone numerous redox cycles. This hypothesis could be used to explain disparate Sc speciation in laterites from different regions reported previously (Chassé et al., 2017; Muñoz et al., 2017; Ulrich et al., 2019; Qin et al., 2020).

During the formation of laterite, the weathering of ferrous ultramafic-mafic rocks and smectite can release aqueous Fe(II), although Fe(II) can be rapidly oxidized and precipitated as Fe(III) (oxyhydr)oxide minerals (Beukes et al., 2002; Yamaguchi et al., 2007, Wu et al., 2019). In addition, under anaerobic conditions in water-saturated environment, Fe(III) can be used as an alternate electron acceptor by dissimilatory Fe-reducing bacteria to produce soluble Fe(II) in solution, which is transported within the soil by advective and diffusive processes (e.g., Lovley et al., 2004; Wiederhold et al., 2007, Li et al., 2017). Thus, aqueous Fe(II) can be present during lateritization because of the weathering of ferrous rocks and abiotic/microbial Fe reduction under reducing conditions, which would affect the speciation and (re)partitioning of Sc in goethite in the lateritic environment.

We can assume that Sc released from the weathering of parent rocks is initially adsorbed by newly formed goethite during lateritization, as the adsorbed Sc species in million-year-old laterites may result from the original sorption mechanism (Chassé et al., 2019, 2020). For the laterites from Australian Syerston–Flemington deposits, Chassé

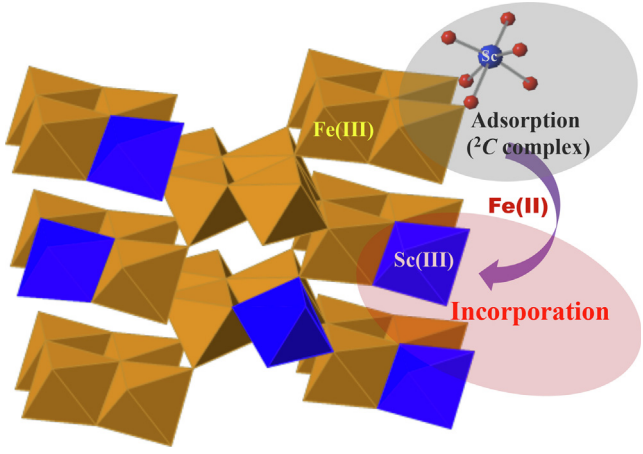

Fig. 12. Schematic diagram showing that adsorbed Sc on the goethite surface (bidentate-binuclear corner-sharing complex, ^2C) is incorporated into the crystal structure (substitution for Fe(III)) in the presence of aqueous Fe(II).

et al. (2017) proposed that tectonic stability is one of the key factors affecting the formation of this highest-grade Sc lateritic deposit, which may imply relatively less Fe(II)-Fe(III) redox cycles during lateritic weathering. Hence, the adsorption of predominant Sc on goethite is expected because of the limited influence of Fe(II) on the initial adsorbed species. By contrast, the occurrence of different generations of goethite in the New Caledonia Ni-Co laterites shows that a successive dissolution and recrystallization cycle of goethite have undergone during lateritization (Dublet et al., 2015; Teitler et al., 2019; Ulrich et al., 2019), which could play a significant role in the remobilization and redistribution of Sc and Ni in laterites. The dominant Sc incorporated into goethite in Ni-Co laterites from New Caledonia (Muñoz et al., 2017; Ulrich et al., 2019) may be attributed to the process that the original adsorbed Sc becomes progressively incorporated into the interior of goethite during the successive goethite recrystallization possibly promoted by aqueous Fe(II).

As for the Philippine Ni laterite, the Sc μ-XAFS results of goethite particles from the present study indicate that most of Sc (69–79%) is incorporated into the crystal structure. Previous bulk Sc XANES analysis of the same sample (LS-1) showed that the ratios of Sc-substituted species into the goethite structure and Sc-adsorbed species on the goethite surface were 60% and 40% (Qin et al., 2020). The higher ratio of Sc-substituted species from μ-XAFS analysis is not surprising, as the two μ-XAFS spectra were collected from the Sc-rich goethite hotspots, in which Sc incorporation could be expected to be relatively larger. By comparison, the bulk XANES gives the average speciation information, which could include the goethite particles with higher Sc adsorption species. However, both the bulk and μ-XAFS results demonstrate that a part of Sc (up to 80%) can be incorporated into the crystal structure of goethite in natural laterite samples from the Philippines, in addition to the adsorption of Sc onto goethite. This finding may be also interpreted by the effect of Fe(II)-catalyzed recrystallization on Sc speciation in goethite, but the Fe(II) redox cycles may be not so frequent during the formation of Philippine laterite compared with the laterites in New Caledonia. A recent study (Li et al., 2017) has suggested that the transport of aqueous Fe(II) species could be spatially limited under reducing situations for the laterites in Southern Philippines in tropical environments, based on a small Fe isotopic fractionation and significant Fe loss during the formation of laterites.

Therefore, the redox-driven goethite recrystallization induced by aqueous Fe(II) could control the Sc speciation and repartitioning between the goethite surface and bulk of the mineral in the lateritic environment. Nonetheless, this recrystallization process could also involve simultaneous dissolution of goethite surfaces, which may cause the possible release of the trace elements incorporated into goethite from the regions undergoing Fe(III) reductive dissolution in the presence of aqueous Fe(II) (e.g., Frierdich et al., 2011, 2019a). Further studies are needed to clarify the effect of dynamic goethite recrystallization induced by aqueous Fe(II) on Sc speciation and partitioning behavior in various environments.

5. CONCLUSIONS

This study elucidates the molecular-scale mechanisms for Sc immobilization by surface adsorption on and structural incorporation into goethite. Sc is preferentially adsorbed on the corner-sharing sites of the goethite surface via the bidentate-binuclear inner-sphere complexation, while Sc is incorporated into the crystal structure via isomorphous substitution for Fe(III) in goethite. Furthermore, we demonstrate that the adsorbed Sc on the goethite surface can be incorporated into the goethite lattice in the presence of aqueous Fe(II), which possibly controls the speciation and partitioning of Sc in the lateritic environment. These findings provide critical insights into the understanding of geochemical behavior and environmental fates of Sc. Our study also has implications for designing optimal mining protocol for Sc recovery in laterites.

Declaration of Competing Interest

The authors declare that they have no known competing financial interests or personal relationships that could have appeared to influence the work reported in this paper.

ACKNOWLEDGMENTS

This work was supported by the National Natural Science Foundation of China (Nos. U1732132 and 41303099) and JSPS KAKENHI (Nos. 20K15204, 19H01960, and 19K21893). This study was performed with the approval of Photon Factory (Nos. 2018G575 and 2018G089).

APPENDIX A. SUPPLEMENTARY MATERIAL

Supplementary data to this article can be found online at https://doi.org/10.1016/j.gca.2020.11.020.

REFERENCES

Alvarez M., Rueda E. H. and Sileo E. E. (2007) Simultaneous incorporation of Mn and Al in the goethite structure. *Geochim. Cosmochim. Acta* **71**, 1009–1020.

Beukes N. J., Dorland H., Gutzmer J., Nedachi M. and Ohmoto H. (2002) Tropical laterites, life on land, and the history of atmospheric oxygen in the Paleoproterozoic. *Geology* **30**, 491–494.

Boily J. F., Lutzenkirchen J., Balmes O., Beattie J. and Sjoberg S. (2001) Modelling proton binding at the goethite (α-FeOOH)-water interface. *Coll. Surf. A* **179**, 11–27.

Brown G. and Calas G. (2013) Mineral-aqueous solution interfaces and their impact on the environment. *Geochem. Perspect.* **1**, 545–560.

BurleSon D. J. and Penn R. I. (2006) Two-step growth of goethite from ferrihydrite. *Langmuir* **22**, 402–409.

Burton E. D., Hockmann K. and Karimian N. (2020) Antimony sorption to goethite: effects of Fe(II)-catalyzed recrystallization. *ACS. Earth. Space. Chem.* **4**, 476–487.

Carvalho-e-Silva M. L., Ramos A. Y., Tolentino H. C. N., Enzweiler J., Netto S. M. and Alves M. D. C. M. (2003) Incorporation of Ni into natural goethite: An investigation by X-ray absorption spectroscopy. *Am. Mineral.* **88**, 876–882.

Catalano J. G., Luo Y. and Otemuyiwa B. (2011) Effect of aqueous Fe(II) on arsenate sorption on goethite and hematite. *Environ. Sci. Technol.* **45**, 8826–8833.

Catalano J. G., Park C., Fenter P. and Zhang Z. (2008) Simultaneous inner- and outer-sphere arsenate complexation on corundum and hematite. *Geochim. Cosmochim. Acta* **72**, 1986–2004.

Chassé M., Blanchard M., Cabaret D., Juhin A., Vantelon D. and Calas G. (2020) First-principles modeling of X-Ray absorption spectra enlightens the processes of scandium sequestration by iron oxides. *Am. Mineral.* **105**, 1099–1103.

Chassé M., Griffin W. L., O'Reilly S. Y. and Calas G. (2017) Scandium speciation in a world-class lateritic deposit. *Geochem. Perspect. Lett.* **3**, 105–114.

Chassé M., Griffin W. L., O'Reilly S. Y. and Calas G. (2019) Australian laterites reveal mechanisms governing scandium dynamics in the critical zone. *Geochim. Cosmochim. Acta* **260**, 292–310.

Chassé M., Juhin A., Cabaret D., Delhommaye S., Vantelon D. and Calas G. (2018) Influence of crystallographic environment on scandium K-edge X-ray absorption near-edge structure spectra. *Phys. Chem. Chem. Phys.* **20**, 23903.

Cotton S. A. (2018) The scandium aqua ion revisited. *Comment. Inorg. Chem.* **38**, 110–125.

Crosby H. A., Roden E. E., Johnson C. M. and Beard B. L. (2007) The mechanisms of iron isotope fractionation produced during dissimilatory Fe(III) reduction by Shewanella putrefaciens and Geobacter sulfurreducens. *Geobiology.* **5**, 169–189.

Domingo C., Rodriguez-Clemente R. and Blesa A. (1994) Morphological properties of α-FeOOH, γ-FeOOH and Fe_3O_4 obtained by oxidation of aqueous Fe(II) solutions. *J. Colloid. Interface. Sci.* **165**, 244–252.

Dublet G., Juillot F., Morin G., Fritsch E., Fandeur D. and Brown G. E. (2015) Goethite aging explains Ni depletion in upper units of ultramafic lateritic ores from New Caledonia. *Geochim. Cosmochim. Acta* **160**, 1–15.

Dzombak D. A. and Morel F. M. M. (1990) *Surface Complexation Modeling: Hydrous Ferric Oxide*. Wiley-Interscience, New York.

Frierdich A. J., Beard B. L., Reddy T. R., Scherer M. M. and Johnson C. M. (2014) Iron isotope fractionation between aqueous Fe(II) and goethite revisited: New insights based on a multi-direction approach to equilibrium and isotopic exchange rate modification. *Geochim. Cosmochim. Acta* **139**, 383–398.

Frierdich A. J., Luo Y. and Catalano J. G. (2011) Trace element cycling through iron oxide minerals during redox-driven dynamic recrystallization. *Geology* **39**, 1083–1086.

Frierdich A. J., McBride A., Tomkinson S. and Southall S. C. (2019a) Nickel cycling and negative feedback on Fe(II)-catalyzed recrystallization of goethite. *ACS. Earth. Space. Chem.* **3**, 1932–1941.

Frierdich A. J., Saxey D. W., Adineh V. R., Fougerouse D., Reddy S. M., Rickard W. D. A., Sadek A. Z. and Southall S. C. (2019b) Direct observation of nanoparticulate goethite recrystallization by atom probe analysis of isotopic tracers. *Environ. Sci. Technol.* **53**, 13126–13135.

Frisch M. J., Trucks G. W., Schlegel H. B., Scuseria G. E., Robb M. A., Cheeseman J. R., Scalmani G., Barone V., Mennucci B., Petersson G. A., Nakatsuji H., Caricato M., Li X., Hratchian H. P., Izmaylov A. F., Bloino J., Zheng G., Sonnenberg J. L., Hada M., Ehara M., Toyota K., Fukuda R., Hasegawa J., Ishida M., Nakajima T., Honda Y., Kitao O., Nakai H., Vreven T., Montgomery Jr J. A., Peralta J. E., Ogliaro F., Bearpark M., Heyd J. J., Brothers E., Kudin K. N., Staroverov V. N., Kobayashi R., Normand J., Raghavachari K., Rendell A., Burant J. C., Iyengar S. S., Tomasi J., Cossi M., Rega N., Millam N. J., Klene M., Knox J. E., Cross J. B., Bakken V., Adamo C., Jaramillo J., Gomperts R., Stratmann R. E., Yazyev O., Austin A. J., Cammi R., Pomelli C., OchterskiJ. W., Martin R. L., Morokuma K., Zakrzewski V. G., Voth G. A., Salvador P., Dannenberg J. J., Dapprich S., Daniels A. D., Farkas O., Foresman J. B., Ortiz J. V., Cioslowski J. and Fox D. J. (2009) Gaussian09 Revision D.01. GaussianInc., Wallingford, CT.

Gao Y., Kan A. T. and Tomson M. B. (2003) Critical evaluation of desorption phenomena of heavy metals from natural sediments. *Environ. Sci. Technol.* **37**, 5566–5573.

Gorski C. A. and Fantle M. S. (2017) Stable mineral recrystallization in low temperature aqueous systems: A critical review. *Geochim Cosmochim Acta* **198**, 439–465.

Gualtieri A. F. and Venturelli P. (1999) In situ study of the goethite hematite phase transformation by real time synchrotron powder diffraction. *Am. Mineral.* **84**, 895–904.

Gustafsson J. P. (2018) Visual MINTEQ, version 3.1; Department of Land and Water Resources Engineering, KTH (Royal Institute of Technology): Stockholm. Available for free download at the website of http://vminteq.lwr.kth.se/download/.

Handler R. M., Beard B. L., Johnson C. M. and Scherer M. M. (2009) Atom exchange between aqueous Fe(II) and goethite: An Fe isotope tracer study. *Environ. Sci. Technol.* **43**, 1102–1107.

Handler R. M., Frierdich A. J., Johnson C. M., Rosso K. M., Beard B. L., Wang C., Latta D. E., Neumann A., Pasakarnis T., Premaratne W. A. P. J. and Scherer M. M. (2014) Fe(II)-catalyzed recrystallization of goethite revisited. *Environ. Sci. Technol.* **48**, 11302–11311.

Harada T. and Takahashi Y. (2008) Origin of the difference in the distribution behavior of tellurium and selenium in a soil-water system. *Geochim. Cosmochim. Acta* **72**, 1281–1294.

Hayes K. F., Roe A. L., Brown, Jr., G. E., Hodgson K. O., Leckie J. O. and Parks G. A. (1987) In situ X-ray absorption study of surface complexes: Selenium oxyanions on α-FeOOH. *Science* **238**, 783–786.

Hinkle M. A. G. and Catalano J. G. (2015) Effect of phosphate and sulfate on Ni repartitioning during Fe(II)-catalyzed Fe(III) oxide mineral recrystallization. *Geochim. Cosmochim. Acta* **165**, 62–74.

Ho Y. S. and McKay G. (1999a) Pseudo-second order model for sorption processes. *Process Biochem.* **34**, 451–465.

Ho Y. S. and McKay G. (1999b) A kinetic study of dye sorption by biosorbent waste product pith. *Resour. Conserv. Recy.* **25**, 171–193.

Ho Y. S. and Ofomaja A. E. (2006) Pseudo-second-order model for lead ion sorption from aqueous solutions onto palm kernel fiber. *J. Hazard. Mater.* **129**, 137–142.

Jacob K. T., Raj S. and Rannesh I. (2007) Vegard's law: a fundamental relation or an approximation?. *Int. J. Mater. Res.* **98** 776–779.

Kashiwabara T., Oishi Y., Sakaguchi A., Sugiyama T., Usui A. and Takahashi Y. (2014) Chemical processes for the extreme enrichment of tellurium into marine ferromanganese oxides. *Geochim. Cosmochim. Acta* **131**, 150–163.

Kawamoto T., Fujita K., Yamada I., Matoba T., Kim S. J., Gao P., Pan X., Findlay S. D., Tassel C., Kageyama H., Studer A. J., Hester J., Irifune T., Akamatsu H. and Tanaka K. (2014) Room-temperature polar ferromagnet $ScFeO_3$ transformed from a high-pressure orthorhombic perovskite phase. *J. Am. Chem. Soc.* **136**, 15291–15299.

Kosmulski M., Durand-Vidal S., Maczka E. and Rosenholm J. B. (2004) Morphology of synthetic goethite. *J. Colloid. Interface. Sci.* **271**, 261–269.

Langmuir D. (1997) *Aqueous environmental geochemistry*. Prentice Hall, Upple Saddle River.

Levard C., Borschneck D., Grauby O., Rose J. and Ambrosi J. P. (2018) Goethite, a tailor-made host for the critical metal scandium: the $Fe_xSc_{(1-x)}OOH$ solid solution. *Geochem. Perspect. Lett.* **9**, 16–20.

Li M., He Y. S., Kang J. T., Yang X. Y., He Z. W., Yu H. M. and Huang F. (2017) Why was iron lost without significant isotope fractionation during the lateritic process in tropical environments? *Geoderma* **290**, 1–9.

Lindqvist-Reis P., Persson I. and Sandstrom M. (2006) The hydration of the scandium(III) ion in aqueous solution and crystalline hydrates studied by XAFS spectroscopy, large-angle X-ray scattering and crystallography. *Dalton. Trans.* **32**, 3868–3878.

Liu H., Lu X., Li M., Zhang L., Pan C., Zhang R., Li J. and Xiang W. (2018) Structural incorporation of manganese into goethite and its enhancement of pb(II) adsorption. *Environ. Sci. Technol.* **52**, 4719–4727.

Lovley D. R., Holmes D. E. and Nevin K. P. (2004) Dissimilatory Fe(III) and Mn(IV) reduction. *Adv. Microb. Physiol.* **49**, 219–286.

Manceau A., Schlegel M. L., Musso M., Sole V. A., Gauthier C., Petit P. E. and Trolard F. (2000) Crystal chemistry of trace elements in natural and synthetic goethite. *Geochim. Cosmochim. Acta* **64**, 3643–3661.

Mitsunobu S., Takahashi Y., Terada Y. and Sakata M. (2010) Antimony(V) incorporation into synthetic ferrihydrite, goethite, and natural iron oxyhydroxides. *Environ. Sci. Technol.* **44**, 3712–3718.

Muñoz M., Ulrich M., Levard C., Rose J., Ambrosi J.-P., Cathelineau M., Teitler Y., Marcaillou C. and Hesse B. (2017) Distribution and speciation of Sc in lateritic profiles of New Caledonia using synchrotron-XRF and Sc K-edge XANES spectroscopy. In: First International Workshop on the Geochemical Cycle of Nickel, Nancy.

Notini L., Latta D. E., Neumann A., Pearce C. I., Sassi M., N'Diaye A. T., Rosso K. M. and Scherer M. M. (2018) The role of defects in Fe(II)-goethite electron transfer. *Environ. Sci. Technol.* **52**, 2751–2759.

Orberger B. and van der Ent A. (2019) Nickel laterites as sources of nickel, cobalt and scandium: Increasing resource efficiency through new geochemical and biological insights. *J. Geochem. Explor.* **204**, 297–299.

Peacock C. L. and Sherman D. M. (2004) Vanadium(V) adsorption onto goethite (α- FeOOH) at pH 1.5–12: a surface complexation model based on ab initio molecular geometries and EXAFS spectroscopy. *Geochim. Cosmochim. Acta* **68**, 1723–1733.

Poledniok J. (2008) Speciation of scandium and gallium in soil. *Chemosphere* **73**, 572–579.

Qin H. B., Takeichi Y., Nitani H., Terada Y., Harada T. and Takahashi Y. (2017a) Tellurium distribution and speciation in contaminated soils from abandoned mine tailings: Comparison with selenium. *Environ. Sci. Technol.* **51**, 6027–6035.

Qin H. B., Uesugi S., Yang S. T., Tanaka M., Kashiwabara T., Itai T., Usui A. and Takahashi Y. (2019) Enrichment mechanisms of antimony and arsenic in marine ferromanganese oxides: insights from the structural similarity. *Geochim. Cosmochim. Acta* **257**, 110–130.

Qin H. B., Yang S. T., Tanaka M., Sanematsu K., Arcilla C. and Takahashi Y. (2020) Chemical speciation of scandium and yttrium in laterites: New insights into the control of their partitioning behaviors. *Chem. Geol.* **552** 119771.

Qin H. B., Yokoyama Y., Fan Q., Iwatani H., Tanaka K., Sakaguchi A., Kanai Y., Zhu J. M., Onda Y. and Takahashi Y. (2012) Investigation of cesium adsorption on soil and sediment samples from Fukushima Prefecture by sequential extraction and EXAFS technique. *Geochem. J.* **46**, 297–302.

Qin H. B., Zhu J. M., Lin Z. Q., Xu W. P., Tan D. C., Zheng L. R. and Takahashi Y. (2017b) Selenium speciation in seleniferous agricultural soils under different cropping systems using sequential extraction and X-ray absorption spectroscopy. *Environ. Pollut.* **225**, 361–369.

Randall S. R., Sherman D. M., Ragnarsdottir K. V. and Collins C. R. (1999) The mechanism of cadmium surface complexation on iron oxyhydroxide minerals. *Geochim. Cosmochim. Acta* **63**, 2971–2987.

Ravel B. and Newville M. (2005) ATHENA, ARTEMIS, HEPHAESTUS: data analysis for X-ray absorption spectroscopy using IFEFFIT. *J. Synchrotron. Radiat.* **12**, 537–541.

Schwertmann U. and Cornell R. M. (2000) *Iron Oxides in the Laboratory*, second ed. Wiley-VCH.

Sherman D. M., Peacock C. L. and Hubbard C. G. (2008) Surface complexation of U(VI) on goethite (α-FeOOH). *Geochim. Cosmochim. Acta* **72**, 298–310.

Sherman D. M. and Randall S. R. (2003) Surface complexation of arsenic(V) to iron(III) (hydr)oxides: Structural mechanism from ab initio molecular geometries and EXAFS spectroscopy. *Geochim. Cosmochim. Acta* **22**, 4223–4230.

Sileo E. E., Ramos A. Y., Magaz G. E. and Blesa M. A. (2004) Long-range vs. short-range ordering in synthetic Cr-substituted goethites. *Geochim. Cosmochim. Acta* **68**, 3053–3063.

Takahashi Y., Ariga D., Fan Q. and Kashiwabara T. (2015) Systematics of distributions of various elements between ferromanganese oxides and seawater from natural observation, thermodynamics, and structures. In Subseafloor Biosphere Linked to Hydrothermal Systems: TAIGA Concept. Springer, pp. 39–48.

Takahashi Y., Manceau A., Geoffroy N., Marcus M. A. and Usui A. (2007) Chemical and structural control of the partitioning of Co, Ce, and Pb in marine ferromanganese oxides. *Geochim. Cosmochim. Acta* **71**, 984–1008.

Tanaka M., Togo Y. S., Yamaguchi N. and Takahashi Y. (2014) An EXAFS study on the adsorption structure of phenyl-substituted organoarsenic compounds on ferrihydrite. *J. Colloid. Interface. Sci.* **415**, 13–17.

Taylor S. D., Liu J., Zhang X., Arey B. W., Kovarik L., Schreiber D. K., Perea D. E. and Rosso K. M. (2019) Visualizing the iron atom exchange front in the Fe(II)-catalyzed recrystallization of goethite by atom probe tomography. *Proc. Natl. Acad. Sci. USA* **116**, 2866–2874.

Teitler Y., Cathelineau M., Ulrich M., Ambrosi J. P., Munoz M. and Sevin B. (2019) Petrology and geochemistry of scandium in new Caledonian Ni-Co laterites. *J. Geochem. Explor.* **196**, 131–155.

Ulrich M., Cathelineau M., Munoz M., Boiron M.-C., Teitler Y. and Karpoff A.-M. (2019) The relative distribution of critical (Sc, REE) and transition metals (Ni Co, Cr, Mn, V) in some Nilaterite deposits of New Caledonia. *J. Geochem. Explor.* **197**, 93–113.

Geological Survey U. S. (2020) Scandium. In *Mineral Commodity Summaries*. U.S. Geological Survey, Reston, USA, pp. 144–145.

Villalobos M., Escobar-Quiroz I. N. and Salazar-Camacho C. (2014) The influence of particle size and structure on the sorption and oxidation behavior of birnessite: I. Adsorption of As(V) and oxidation of As(III). *Geochim. Cosmochim. Acta* **125**, 564–581.

Vind J., Malfliet A., Bonomi C., Paiste P., Sajó I. E., Blanpain B., Tkaczyk A. H., Vassiliadou V. and Panias D. (2018) Modes of occurrences of scandium in Greek bauxite and bauxite residue. *Miner. Eng.* **123**, 35–48.

Wang W., Pranolo Y. and Cheng C. Y. (2011) Metallurgical processes for scandium recovery from various resources: A review. *Hydrometallurgy* **108**, 100–108.

Weber K. A., Achenbach L. A. and Coates J. D. (2006) Microorganisms pumping iron: Anaerobic microbial iron oxidation and reduction. *Nat. Rev. Microbiol.* **4**, 752–764.

Wiederhold J. G., Teutsch N., Kraemer S. M., Halliday A. N. and Kretzschmar R. (2007) Iron isotope fractionation during pedogenesis in redoximorphic soils. *Soil Sci. Soc. Am. J.* **71**, 1840–1850.

Williams-Jones A. E. and Vasyukova O. V. (2018) The Economic Geology of Scandium, the Runt of the Rare Earth Element Litter. *Econ. Geol.* **113**, 973–988.

Wu C., Chen L., Yang S., Cai Y., Xu L., Wu X., Qin H., Liu Z., Chen L. and Wang S. (2018) Macroscopic, theoretical simulation and spectroscopic investigation on the immobilization mechanisms of Ni(II) at cryptomelane/water interfaces. *Chemosphere* **210**, 392–400.

Wu B., Amelung W., Xing Y., Bol R. and Berns A. E. (2019) Iron cycling and isotope fractionation in terrestrial ecosystems. *Earth-Science. Rev.* **190**, 323–352.

Yamaguchi K. E., Johnson C. M., Beard B. L., Beukes N. J., Gutzmer J. and Ohmoto H. (2007) Isotopic evidence for iron mobilization during Paleoproterozoic lateritization of the Hekpoort paleosol profile from Gaborone, Botswana. *Earth Planet. Sci. Lett.* **256**, 577–587.

Yanina S. V. and Rosso K. M. (2008) Linked reactivity at mineral-water interfaces through bulk crystal conduction. *Science* **320**, 218–222.

Yin H., Wu Y., Hou J., Yan X., Li Z., Zhu C., Zhang J., Feng X., Tan W. and Liu F. (2020) Preference of Co over Al for substitution of Fe in goethite (α-FeOOH) structure: Mechanism revealed from EXAFS, XPS, DFT and linear free energy correlation model. *Chem. Geol.* **532** 119378.

Zabinsky S. I., Rehr J. J., Ankudinov A., Albers R. C. and Eller M. J. (1995) Multiple-scattering calculations of X-ray-absorption spectra. *Phys. Rev. B.* **52**, 2995–3009.

Zhao Y. and Truhlar D. G. (2008) The M06 suite of density functionals for main group thermochemistry, thermochemical kinetics, noncovalent interactions, excited states, and transition elements: two new functionals and systematic testing of four M06-class functionals and 12 other functionals. *Theory Chem. Acc.* **120**, 215–241.

Associate editor: Jeffrey G. Catalano